1 Detergent-free reconstitution of transmembrane proteins in giant liposomes of complex curvature by
2 the Synthetic Membrane Transfer

3 *Hemraj Meena[1,*], Rafal Zdanowicz[1,*], Tobias Bock-Bierbaum[2], Till Stephan[3,4,5,6], Sofie Dorothea Ottsen*
4 *Knudsen [7], Stefan Jakobs[3,4,8], Oliver Daumke[2], Per Amstrup Pedersen[7] and Nicola De Franceschi[1]*

5 *1 IMol Polish Academy of Sciences, Warsaw, Poland*

6 *2 Structural Biology, Max Delbrück Center for Molecular Medicine in the Helmholtz Association (MDC),*
7 *Berlin, Germany*

8 *3 Research Group Mitochondrial Structure and Dynamics, Max Planck Institute for Multidisciplinary*
9 *Sciences, Göttingen, Germany.*

10 *4 High Resolution Microscopy, Clinic for Neurology, University Medical Center Göttingen, Göttingen,*
11 *Germany.*

12 *5 Buchmann Institute for Molecular Life Sciences, Goethe University Frankfurt am Main, Germany.*

13 *6 Institute of Molecular Biosciences, Goethe University Frankfurt am Main, Germany.*

14 *7 Department of Biology, University of Copenhagen, Copenhagen, Denmark*

15 *8 Translational Neuroinflammation and Automated Microscopy, Fraunhofer Institute for Translational*
16 *Medicine and Pharmacology ITMP, Göttingen, Germany.*

17 ** Equal contribution*

18

21

22 **Abstract**

23 Transmembrane proteins perform many crucial functions in the cell, including transfer of matter and
24 information across the membrane. Giant Unilamellar Vesicles (GUVs) are the ideal tool for studying these
25 processes; yet functional transmembrane protein reconstitution in GUVs still represents a bottleneck in
26 bottom-up synthetic biology. Here, we developed a novel approach that we call Synthetic Membrane
27 Transfer (SMT), where transmembrane proteins reconstituted into styrene-maleic acid particles in a
28 detergent-free environment can be transferred to the GUV membrane. The SMT approach is a one-step,
29 facile and general method that works for structurally diverse proteins, and it does not require any specific
30 lipid or buffer composition. Moreover, the SMT is fully compatible with the Synthetic Membrane Shaper
31 (SMS) technology, which allows to deform GUVs in a controlled fashion, obtaining dumbbell-shaped GUVs
32 exhibiting a catenoid-like geometry. The combination of SMT and SMS results in functional reconstitution
33 of transmembrane proteins in catenoid membrane necks. Using this approach, we demonstrate that
34 Mic10, a component of the MICOS complex, directly senses membrane curvature and localizes at the neck

35   of dumbbells GUVs, a geometry that recapitulates the shape of mitochondria cristae junctions. This paves

36   the way for bottom-up reconstitution of the MICOS complex on a physiological membrane geometry.

37

38

39   **Introduction**

40   Transmembrane proteins are essential components of biological membranes. They perform a number of

41   crucial tasks, including energy generation (Salmonowicz, 2025), active and passive transport (Alam, 2023),

42   information transfer and signaling (Ripoll, 2025) and the ability to organize protein complexes (Nakamura,

43   2024). Giant Unilamellar Vesicles (GUVs) constitute a versatile platform to study the function of both

44   transmembrane and membrane-associated proteins, (Litschel, 2021) as well as a preferred chassis

45   towards the assembly of synthetic cells (Olivi, 2021). Thanks to their large size, GUVs can be imaged in

46   real time by fluorescent microscopy, allowing tracking of fluorescent molecules translocating across the

47   membrane (Fragasso, 2021). Generating GUVs composed exclusively of phospholipids is relatively easy

48   and can be accomplished by several techniques, including gel-assisted swelling, electroformation, and

49   inverted emulsion (Litschel, 2021). In contrast, functional reconstitution of transmembrane proteins in

50   GUVs is one of the major bottlenecks in bottom-up synthetic biology. This has been achieved in a limited

51   number of cases using different approaches, each one having specific drawbacks. The most established

52   technique is electroformation (Aimon, 2011), but it requires extensive case-by-case optimization and, like

53   all methods based on swelling, suffers from limited encapsulation efficiency (Litschel, 2021). This becomes

54   critical when soluble macromolecules need to be co-encapsulated in the lumen. Reconstitution

55   methodologies based on SUVs-GUVs fusion (Biner, 2016) require the use of cationic lipids: these are non-

56   physiological and may affect protein function.

57   Recently, nanodiscs (NDs) have emerged as an exciting new platform for the structural characterization

58   of transmembrane proteins (Sligar, 2021). NDs are discoidal patches of lipid bilayers with a diameter

59   ranging between 8 and 16 nm that are stabilized by antiparallel belts of membrane scaffold protein (MSP)

60   (Denisov, 2016). An approach for transmembrane protein reconstitution based on Ca^{2+}-mediated fusion

61   of MSP-based NDs with GUVs has been recently developed (Stępień, 2023). This approach requires the

62   target GUV membrane to contain at least 75% of anionic lipids: in addition to making GUVs production

63   very challenging, the combination of such heavily charged membrane with the relatively high Ca^{++}

64   concentration required for achieving fusion makes the system prone to aggregation. Thus, a facile and

65   general method for functional transmembrane protein reconstitution in GUVs using mild conditions and

66   physiological membrane compositions is still missing.

67   In addition to MSP-based NDs, a wide range of synthetic polymer-based lipid particles, whose properties

68   can be finely tuned by design, are available. A prominent class of such polymers are styrene-maleic acid

69   (SMA) copolymers, which are able to extract lipid patches from an intact membrane, generating polymer-

70   stabilized nanoparticles called SMALPs (SMA Lipid Particles) (Kuyler, 2025). While MSP-based NDs exhibit

71   limited interparticle lipid transfer (Stępień, 2023), SMALPs allow fast lipid exchange (Cuevas, 2017).

72   Indeed, SMALPs have been used to transfer transmembrane proteins into nanometer-sized synthetic

73   polymersomes (Catania, 2022).

74   Here, we exploit the lipid exchange property of SMA to develop a novel method for transmembrane

75   protein reconstitution in GUVs composed of phospholipids. We named this method Synthetic Membrane

76   Transfer (SMT). The SMT does not require any specific membrane nor buffer composition, while being

77 compatible with standard membrane compositions widely used in synthetic biology. The SMT is based on
78 inverted emulsion, allowing easy encapsulation of macromolecules in the lumen, overcoming the
79 limitations of existing methods. Here, we demonstrate functional reconstitution of three transmembrane
80 proteins with diverse structural features, including β-barrels, α-helices and membrane-spanning hairpins.
81
82 GUVs have been used extensively to study how proteins preferentially bind to membranes having a
83 specific curvature, using the tube pulling technique (Morlot, 2012; Prévost, 2017; Schöneberg, 2018), or,
84 more recently, the Synthetic Membrane Shaper (SMS) approach (De Franceschi, 2022; De Franceschi,
85 2024). In the SMS approach, GUVs are generated by inverted emulsion, while simultaneously they are
86 being reshaped into "stomatocyte" or "dumbbell" shapes by the action of small DNA assemblies called
87 "nanostars". The crucial feature of both dumbbells and stomatocytes is the presence of a membrane neck
88 having a catenoid shape (also referred to as "saddle" geometry) (Supplementary Figure 1).
89 It is well established that membrane-associated proteins are able to sense and generate membrane
90 curvature: examples include ESCRT-III subunits (Bertin, 2020; Jukic, 2022; De Franceschi, 2018) and BAR-
91 domain proteins (Prévost, 2015). Likewise, a number of transmembrane proteins are expected to
92 generate membrane curvature. These include for instance caveolins (Matthaeus, 2022) and reticulons
93 (Voeltz, 2006; Power, 2017). However, direct evidence for membrane curvature-sensing capability of
94 transmembrane proteins are relatively scant: for instance, tetraspanins have been shown to prefer
95 positively curved membranes over flat ones, but this was done in the context of plasma membrane-
96 derived giant vesicles (Dharan, 2022), thus this sensing capability cannot be unequivocally assigned to the
97 tetraspanins themselves. Only one transmembrane protein - the potassium channel KvAP - has been
98 shown in reconstitution studies in GUVs to directly sense membrane curvature (Aimon, 2014). To the best
99 of our knowledge, there is no direct evidence of transmembrane proteins sensing catenoid-shaped
100 membranes. Yet, many candidates could fall in this category: the Pom121 and Ndc1 subunits of the
101 nuclear pore complex (Funakoshi, 2011; Amm, 2023), thought to mediate the initial steps of nuclear pore
102 formation or the stabilization of high membrane curvature at the nuclear pore; SARS-CoV-2 nsp3 and
103 nsp4, forming a pore in double-membrane vesicles (Huang, 2024), the chemoreceptor TlpA from *B. subtilis*
104 (Strahl, 2015), and the Mic10 subunit of the mitochondrial contact site and organizing system (MICOS)
105 complex (Barbot, 2015; Bohnert, 2015). MICOS is an evolutionarily conserved, multi-subunit complex that
106 has been shown to govern the formation and maintenance of mitochondrial crista junctions featuring a
107 funnel or slit-like architecture (recently reviewed in (Daumke, 2025)). It consists of at least six distinct
108 subunits which are mostly small, membrane-embedded proteins of the inner mitochondrial membrane.
109 Mic10 is thought to form a small hairpin-like structure in the inner mitochondrial membrane which
110 oligomerizes in arc-like structures to stabilize the high curvature of the crista neck (Barbot, 2015; Bohnert,
111 2015). The paucity of reconstitution studies on this topic is likely due to the technical challenges in
112 reconstituting transmembrane proteins while at the same time being able to manipulate the membrane
113 into a catenoid shape.
114 Here, we combine the SMT and SMS technologies in a single-step protocol to overcome the above-
115 mentioned bottlenecks and achieve transmembrane protein reconstitution in GUVs of complex catenoid
116 geometry. This allows probing the curvature-sensing capability of transmembrane proteins in a very
117 simple setup. Using this approach, we show that the MICOS subunit Mic10 senses membrane curvature
118 and becomes enriched in catenoid-shaped necks. This study paves the way for functional reconstitution
119 of large protein complexes that include transmembrane proteins at regions of complex membrane
120 curvature, such as the MICOS complex.

121

122

123 **Results**

124 **Establishing the SMT approach to transfer phospholipids from SMA into GUVs**

125 The rationale behind the SMT approach is that both lipids and transmembrane proteins can be transferred
126 to a GUV membrane simply by the intrinsic propensity of SMA to exchange material (Cuevas, 2017),
127 avoiding the use of detergents or fusogenic agents. Hereafter, we refer to lipids and proteins embedded
128 in SMA as lipid-SMA and protein-SMA, respectively. Initially, we tested whether lipid-SMA could be
129 incorporated into the GUV membrane. In the SMT approach, GUVs are generated by emulsification of an
130 inner solution within an oil phase containing lipids. The emulsion is then layered on top of an outer
131 solution. As the droplets sink by gravity, they first acquire the inner monolayer and finally the outer
132 monolayer as they cross the oil/outer buffer interface (Figure 1A). In order to promote phospholipid
133 insertion into the membrane, lipid-SMA are included in the inner buffer. The high degree of confinement
134 in emulsified droplets is expected to promote interaction between lipid-SMA and the membrane that is
135 being formed. Moreover, the fact that lipid-SMAs are present during the process of membrane formation
136 is expected to lower the energy barrier for insertion and fusion, leading to incorporation of the
137 phospholipids in the GUV membrane. Lipid-SMA were generated by addition of SMA to multilamellar
138 liposomes, which caused the liposome suspension, initially turbid, to clarify. Size-exclusion
139 chromatography indicates that addition of SMA to multilamellar liposomes resulted in a homogeneous
140 population of lipid-SMA, eluting as a single sharp peak (Figure 1B). Inclusion of lipid-SMA, containing the
141 fluorescent lipid Rhodamine-PE, in the inner solution resulted in a high yield of GUVs displaying bright
142 fluorescent signal that colocalized with the GUV membrane (Figure 1C). The fluorescent signal was
143 uniform along the rim, as would be expected if the lipids initially contained in the lipid-SMA had indeed
144 become an integral part of the membrane. In contrast, inclusion of Small Unilamellar Vesicles (SUVs) in
145 the inner buffer without SMA resulted in the SUVs being either retained in the lumen or aggregating on
146 the membrane (Supplementary Figure 2). To avoid any potential cross-talk between fluorescent channels
147 during imaging, Rhodamine-PE was included only in the lipid-SMA. Indeed, in the absence of lipid-SMA,
148 the GUV membrane did not display any detectable fluorescence (Supplementary Figure 3). Moreover,
149 lipid-SMA incorporation in the membrane was concentration-dependent: at low concentration, only the
150 membrane displayed fluorescent signal. As the lipid-SMA concentration was increased, the fluorescent
151 signal at the membrane was accompanied by the signal from lipid-SMA floating in the lumen, indicating
152 that the membrane was being saturated with lipid-SMA (Figure 1D). Overall, these data are consistent
153 with the incorporation of lipid-SMA into the GUV membrane. To shed light on the mechanism of lipid
154 transfer, we imaged the droplets generated during emulsification. We did not observe enrichment of lipid-
155 SMA at the rim of droplets, irrespectively of the lipid-SMA concentration (Supplementary Figure 4). This
156 indicates that association of lipid-SMA with the membrane, and thus lipid transfer, likely happens at the
157 interface between the oil and the outer buffer, while the full bilayer is being formed. It has been previously
158 shown that droplets can remain stationary at the interface for a prolonged time, even upon application
159 of a centrifugal force (Van de Cauter, 2024). Because in the SMT the droplets sink simply by gravity, they
160 likely linger at the interface even longer, leaving enough time for lipid-SMA to interact with the membrane
161 and exchange lipids. This mechanism appears to be particularly relevant during the reconstitution of
162 transmembrane proteins (see following sections). To ensure the correct positioning of the ectodomains,

163 transmembrane proteins require aqueous compartments on both sides of the membrane, a condition that
164 is met when the bilayer forms at the oil/outer buffer interface.

165 **Reconstitution of maltoporin in GUVs by the SMT**
166 Having an initial indication that phospholipids can be exchanged with the GUV membrane, we tested
167 whether the SMT can result in reconstitution of transmembrane proteins. As the first candidate we chose
168 maltoporin, a well-characterized β-barrel transmembrane protein (Ranquin, 2004). We purified
169 maltoporin using n-dodecyl-ß-D-maltoside (DDM)-mediated extraction and subsequently exchanged the
170 detergent with SMA by incubating the sample with bio-beads, obtaining maltoporin-SMA. Thus, the
171 protein that is being reconstituted in GUVs is detergent-free. We also tested incorporation of maltoporin
172 into amphipol A8-35 (hereafter called Apol), a polymer widely used in structural biology (Zubcevic 2016,
173 McDowell 2020, Flegler 2020). Both maltoporin-SMA and maltoporin-Apol eluted as sharp peaks in size-
174 exclusion chromatography, having an apparent molecular weight similar to that of lipid-SMA (Figure 2A).
175 This is in line with the fact that maltoporin does not possess large ectodomains which would affect its
176 elution profile. However, maltoporin-SMA and maltoporin-Apol appeared starkly different when imaged
177 by negative-staining electron microscopy. Maltoporin-SMA formed particles with a narrow size
178 distribution (average size = 12.2 ± 1.3 nm). This is consistent with trimeric maltoporin given its
179 approximate size of 8 nm (Yvonnesdotter, 2023), the SMA belt around the complex, and the effect of
180 uranyl acetate deposition. In contrast, maltoporin-Apol polymerized into long filaments (Figure 2B).
181 Because maltoporin filaments were never reported, we characterized them by cryo-EM. 2D classification
182 and 3D reconstruction confirmed that maltoporin maintained its trimeric form when reconstituted in Apol
183 (Supplementary Figure 5A and 5B), similar to the published structures obtained in detergent
184 (Yvonnesdotter, 2023). Within the filament, however, each trimer constitutes a "unit" capable of
185 polymerizing, an effect seemingly induced by the ApolA8-35 polymer and likely not representing a
186 physiological state of the protein. Nevertheless, we tested the ability of both maltoporin-SMA and
187 maltoporin-Apol to transfer maltoporin to the GUV membrane.
188 We covalently labelled maltoporin using Alexa-488 and performed the SMT procedure by including
189 maltoporin in the inner buffer. With maltoporin-SMA we obtained GUVs displaying a relatively
190 homogeneous fluorescent signal at the membrane (Figure 2C, 2D). The fluorescent signal was due to the
191 reconstituted maltoporin, since inclusion of SMA alone in the inner buffer did not result in any detectable
192 fluorescence signal in the 488 nm channel (Supplementary Figure 6A). In contrast, maltoporin-Apol failed
193 to achieve protein incorporation in the GUV membrane (Figure 2E). This indicates that the choice of the
194 polymer used to embed the protein plays a critical role, and this difference may be potentially due to the
195 formation of supramolecular assemblies that may negatively impact reconstitution (i.e. maltoporin
196 filaments). Similar to lipid-SMA, maltoporin-SMA could also saturate the GUV membrane by increasing its
197 concentration in the inner buffer (Supplementary Figure 6B).
198 Next, we tested whether maltoporin was functionally reconstituted. To this end, we examined its ability
199 to transport maltose by visualizing osmotically-induced deformation of GUVs. In this assay, GUVs
200 generated in iso-osmotic outer buffer are subsequently perfused using a microfluidics capillary with a
201 buffer having a higher osmolarity, which is achieved by adding 200 mM maltose to the iso-osmotic outer
202 buffer. Because maltose cannot cross the membrane, GUVs generated in the absence of maltoporin
203 experience an osmotic imbalance, resulting in membrane deformation and deviation from a spherical
204 shape. In contrast, functionally reconstituted maltoporin allows transfer of maltose across the membrane,
205 nullifying the osmotic imbalance and resulting in GUVs that remain spherical (Figure 2F). These data
206 indicate that maltoporin has been functionally reconstituted.

207

208

Reconstitution of aquaporin-12 in GUVs by the SMT

Next, we tested reconstitution of an all-α-helical transmembrane protein, aquaporin-12 (AQP12). We purified GFP-tagged AQP12 by DDM + cholesteryl hemisuccinate (CHS) extraction and exchanged the detergent with SMA. The resulting AQP12-SMA eluted as larger species than lipid-SMA in size-exclusion chromatography (Figure 3A), likely due to the presence of the GFP tag. AQP12-SMA gave particles with an average size of 14.2 ± 2.2 nm in negative-staining EM (Figure 3B). These results are consistent with AQP12 being reconstituted in an oligomeric state, since AQP12 monomers are only 3 nm wide (Verkman, 2000). Upon reconstitution using the SMT procedure, GUVs with relatively homogeneous GFP signal at the membrane were obtained (Figure 3C, 3D).

The functionality of AQP12, a water and glycerol transporter, has been previously demonstrated by measuring the size of proteo-SUVs upon addition of glycerol using stopped-flow dynamic light scattering (DLS) (Bjørkskov, 2017). However, this approach cannot be used for GUVs as their size exceeds the range of DLS and GUVs observation is not compatible with the use of a stopped-flow device. Since there are no commercially available fluorescent sensors for glycerol, we tested AQP12 functionality as an H_2O_2 transporter. We generated GUVs by including an H_2O_2 fluorescent sensor in the inner buffer. Because some droplets generated during emulsification fail to become GUVs, some of the inner buffer is released into the outer buffer. Therefore, the sensor is also present in the outer buffer. We then injected H_2O_2 directly into the observation chamber using a microfluidics capillary. As H_2O_2 progressively entered the chamber, an increase in fluorescence from the sensor was recorded in bulk (Supplementary Figure 7). Since we noticed that the presence of SMA alone in the inner buffer resulted in partial permeabilization of the membrane to H_2O_2 (Supplementary Figure 8), we included SMALP200 in our negative control. We detected an increased influx of H_2O_2 in the AQP-12 sample compared to the SMA-only control (Figure 3E). These data indicate that AQP12 was functionally reconstituted using the SMT protocol. Importantly, the SMT appears to be a general method that allows both β-barrel and α-helical proteins to be reconstituted with minimal optimization required.

Versatility of the SMT approach

To investigate the applicability of the SMT approach for synthetic biology, we tested transmembrane proteins reconstitution using lipid compositions and co-encapsulation with macromolecules commonly employed in bottom-up reconstitution studies.

Negatively charged lipids such as DOPS (1,2-dioleoyl-sn-glycero-3-phospho-L-serine) are often included in GUVs to promote protein binding (Mercier, 2020). We tested maltoporin incorporation upon increasing amount of DOPS in the GUVs membrane. We found that while reconstitution using the SMT is only marginally affected by the presence of up to 15% of DOPS, the efficiency starts to decline at 30% and above (Figure 4A). This is likely due to the fact that the SMA polymer is itself negatively charged. However, a concentration of negatively charged lipids lower than 30% is typically used to trigger protein binding (Schöneberg, 2018). Thus, the SMT is compatible with the presence of negatively charged lipids, while at the same time it does not require any specific lipid composition to promote reconstitution.

The grand goal of synthetic biology is to build a synthetic cell from the bottom-up: this requires encapsulation of a combination of macromolecules having a high degree of complexity. This is typically achieved by combining nucleic acids, proteins and carbohydrates. Here, we demonstrate that transmembrane protein reconstitution via the SMT approach is compatible with co-encapsulation of these macromolecules. 10 kDa dextran (Figure 4B), bovine serum albumin (BSA) (Figure 4C) and a 22-mer single

251   strand DNA (ssDNA) (Figure 4D) could be co-encapsulated with maltoporin without affecting transfer of
252   the transmembrane protein to the GUV membrane and without compromising the solubility of these
253   macromolecules. These data demonstrate the versatility of the SMT approach for encapsulation of
254   different classes of macromolecules with concomitant transmembrane protein reconstitution,
255   highlighting its potential in bottom-up reconstitution studies.
256

Functional reconstitution of Mic10 at the neck of dumbbell-shaped GUVs

257
258   Finally, we combined transmembrane protein reconstitution with membrane deformation by
259   reconstituting Mic10, a transmembrane hairpin protein and one of the key components of the MICOS
260   complex at the crista junctions in mitochondria (Stephan, 2020). Mic10 is known to oligomerize in the
261   membrane (Barbot, 2015; Bohnert, 2015, Stephan, 2024), forming stable and robust higher order
262   assemblies, making it a challenging candidate for functional and structural studies. To obtain the protein
263   in a functional form, we pursued an approach described for stabilizing the flexible termini of a vitamin K
264   epoxide reductase (Liu, 2021). Thus, we recombinantly produced and purified *Drosophila* Mic10b
265   (Stephan, 2024) in DDM as a split GFP-fusion protein, in which both the N- and C-termini were fused to
266   the two moieties of split-GFP. The DDM was exchanged with SMA, obtaining Mic10-SMA that was
267   subjected to size-exclusion chromatography (Figure 5A). The larger apparent size of Mic10-SMA compared
268   to lipid-SMA may be attributed to the presence of the GFP tag or to the formation of Mic10 oligomers.
269   Upon reconstitution using SMT, Mic10 appeared in clusters that were freely diffusing on the membrane
270   (Figure 5B, 5C and Movie 1). The membrane could also be saturated with Mic10 upon increasing protein
271   concentration (Figure 5D). Interestingly, we found that the optimal Mic10 concentration to obtain well-
272   defined clusters was 150 nM: this is similar to the concentration used to obtain neck-localized clusters of
273   dynamin A in a previous study (De Franceschi, 2024). At a concentration of 75 nM, Mic10 also localized at
274   the membrane, however, it exhibited a more diffuse pattern possibly due to inefficient clustering of the
275   protein at lower density.
276   We then tested whether Mic10 could be reconstituted while deforming the GUVs into a dumbbell shape.
277   We performed Mic10 reconstitution by the SMT in hyperosmotic conditions and by adding cholesterol-
278   functionalized nanostars in the outer buffer, which induce GUV deformation into a dumbbell shape and
279   generate membrane necks (De Franceschi, 2022). For this set of experiments, we included DOPE-
280   Rhodamine in the GUV membrane for clearer visualization of membrane necks. We observed a stable
281   localization of Mic10 clusters at the neck of dumbbell liposomes (Figure 5E, Supplementary Figure 9A and
282   Movie 2, Movie 3). Mic10 clusters also localized at the necks of nanotubes emanating from GUVs (Figure
283   5F, Movie 4), as well as along the nanotubes themselves (Supplementary Figure 9B and Movie 5).
284   Occasionally, we also observed long membrane tubes that displayed a very bright GFP signal, indicating a
285   high density of Mic10 (Movie 6). These structures may correspond to the membrane tubes obtained *in*
286   *vivo* upon strong overexpression of Mic10 (Stephan, 2024).
287   Localization at necks and along nanotubes strongly resembles the localization of soluble curvature-sensing
288   proteins such as ESCRT-III components (De Franceschi, 2018; Schöneberg, 2018; Souza, 2025). In contrast,
289   maltoporin was not enriched at the neck of dumbbells (Supplementary Figure 10). Curvature sensing could
290   only be achieved if Mic10 was correctly inserted into the membrane, thereby confirming that Mic10 has
291   been functionally reconstituted.
292

293

294

Discussion

296 We presented an approach called SMT to achieve facile, detergent-free reconstitution of transmembrane
297 proteins in GUVs. We demonstrated successful functional reconstitution of three transmembrane
298 proteins which are structurally diverse – maltoporin is a β-barrel protein, aquaporin-12 is all α-helical,
299 while Mic10 is a membrane-spanning hairpin protein. We also combined transmembrane protein
300 reconstitution with membrane deformation, obtaining Mic10 enrichment at catenoid membrane necks.
301 Such necks recapitulate the shape of mitochondrial crista junctions, where Mic10 localizes. This
302 represents the first example of a transmembrane protein directly sensing a catenoid shape. Overall, the
303 findings reported here portray the SMT as a promising platform for reconstituting large protein complexes
304 by a bottom-up approach, when such complexes include transmembrane proteins and are assembled at
305 catenoid necks. These include the MICOS complex (Barbot, 2015; Bohnert, 2015), the nuclear pore
306 complex (Funakoshi, 2011; Amm, 2023), the SARS-CoV-2 nsp3/nsp4 complex (Huang, 2024) and the
307 bacterial Z-ring (Du, 2019), just to name a few (Figure 5G). These systems are notoriously challenging to
308 reconstitute using the state-of-the-art techniques. An additional advantage of the SMT is that it does not
309 require sophisticated equipment and it is very easy to perform with minimal training and optimization.
310 We anticipate that the SMT may become widely adopted as a general platform in the synthetic biology
311 community.

Author Contributions

313 N.D.F conceived the research. H.M. and N.D.F. set up the SMT protocol. H.M. and N.D.F. performed the
314 SMT and carried out the microscopy experiments. R.Z. collected and analyzed the EM data. R.Z. carried
315 out the chromatography. R.Z. wrote and applied the script for rim analysis. R.Z. purified maltoporin.
316 S.D.O.K. and P.A.P. purified aquaporin. T.B.B., T.S., S.J. and O.D. cloned and purified Mic10. N.D.F. wrote
317 the manuscript with input from the all other authors. H.M. and R.Z. contributed equally to this work.

Acknowledgements

333

334

References

336 Aimon S, Manzi J, Schmidt D, Poveda Larrosa JA, Bassereau P, Toombes GE. Functional reconstitution of a
337 voltage-gated potassium channel in giant unilamellar vesicles. PLoS One. 2011;6(10):e25529.

338 Alam S, Doherty E, Ortega-Prieto P, Arizanova J, Fets L. Membrane transporters in cell physiology, cancer
339 metabolism and drug response. Dis Model Mech. 2023 Nov 1;16(11):dmm050404.

340 Amm I, Weberruss M, Hellwig A, Schwarz J, Tatarek-Nossol M, Lüchtenborg C, Kallas M, Brügger B, Hurt
341 E, Antonin W. Distinct domains in Ndc1 mediate its interaction with the Nup84 complex and the nuclear
342 membrane. J Cell Biol. 2023 Jun 5;222(6):e202210059.

343 Barbot M, Jans DC, Schulz C, Denkert N, Kroppen B, Hoppert M, Jakobs S, Meinecke M. Mic10 oligomerizes
344 to bend mitochondrial inner membranes at cristae junctions. Cell Metab. 2015 May 5;21(5):756-63.

345 Bertin A, de Franceschi N, de la Mora E, Maity S, Alqabandi M, Miguet N, di Cicco A, Roos WH, Mangenot
346 S, Weissenhorn W, Bassereau P. Human ESCRT-III polymers assemble on positively curved membranes
347 and induce helical membrane tube formation. Nat Commun. 2020 May 29;11(1):2663.

348 Biner O, Schick T, Müller Y, von Ballmoos C. Delivery of membrane proteins into small and giant unilamellar
349 vesicles by charge-mediated fusion. FEBS Lett. 2016 Jul;590(14):2051-62.

350 Bohnert M, Zerbes RM, Davies KM, Mühleip AW, Rampelt H, Horvath SE, Boenke T, Kram A, Perschil I,
351 Veenhuis M, Kühlbrandt W, van der Klei IJ, Pfanner N, van der Laan M. Central role of Mic10 in the
352 mitochondrial contact site and cristae organizing system. Cell Metab. 2015 May 5;21(5):747-55.

353 Bjørkskov FB, Krabbe SL, Nurup CN, Missel JW, Spulber M, Bomholt J, Molbaek K, Helix-Nielsen C, Gotfryd
354 K, Gourdon P, Pedersen PA. Purification and functional comparison of nine human Aquaporins produced
355 in Saccharomyces cerevisiae for the purpose of biophysical characterization. Sci Rep. 2017 Dec
356 4;7(1):16899.

357 Catania R, Machin J, Rappolt M, Muench SP, Beales PA, Jeuken LJC. Detergent-Free Functionalization of
358 Hybrid Vesicles with Membrane Proteins Using SMALPs. Macromolecules. 2022 May 10;55(9):3415-3422.

359 Cuevas Arenas R, Danielczak B, Martel A, Porcar L, Breyton C, Ebel C, Keller S. Fast Collisional Lipid Transfer
360 Among Polymer-Bounded Nanodiscs. Sci Rep. 2017 Apr 5;7:45875.

361 Daumke O, van der Laan M. Molecular machineries shaping the mitochondrial inner membrane. Nat Rev
362 Mol Cell Biol. 2025 May 14.

363 De Franceschi N, Alqabandi M, Miguet N, Caillat C, Mangenot S, Weissenhorn W, Bassereau P. The ESCRT
364 protein CHMP2B acts as a diffusion barrier on reconstituted membrane necks. J Cell Sci. 2018 Aug
365 3;132(4):jcs217968.

366 De Franceschi N, Pezeshkian W, Fragasso A, Bruininks BMH, Tsai S, Marrink SJ, Dekker C. Synthetic
367 Membrane Shaper for Controlled Liposome Deformation. ACS Nano. 2022 Nov 28;17(2):966–78.

368 De Franceschi N, Barth R, Meindlhumer S, Fragasso A, Dekker C. Dynamin A as a one-component division
369 machinery for synthetic cells. Nat Nanotechnol. 2024 Jan;19(1):70-76.

370 Denisov IG, Sligar SG. Nanodiscs for structural and functional studies of membrane proteins. Nat Struct
371 Mol Biol. 2016 Jun;23(6):481-6.

372 Dharan R, Goren S, Cheppali SK, Shendrik P, Brand G, Vaknin A, Yu L, Kozlov MM, Sorkin R. Transmembrane
373 proteins tetraspanin 4 and CD9 sense membrane curvature. Proc Natl Acad Sci USA. 2022 Oct
374 25;119(43):e2208993119.

375 Du S, Lutkenhaus J. At the Heart of Bacterial Cytokinesis: The Z Ring. Trends Microbiol. 2019 Sep;27(9):781-
376 791.

377 Flegler VJ, Rasmussen A, Rao S, Wu N, Zenobi R, Sansom MSP, Hedrich R, Rasmussen T, Böttcher B. The
378 MscS-like channel YnaI has a gating mechanism based on flexible pore helices. Proc Natl Acad Sci USA.
379 2020 Nov 17;117(46):28754-28762.

380 Fragasso A, De Franceschi N, Stömmer P, van der Sluis EO, Dietz H, Dekker C. Reconstitution of Ultrawide
381 DNA Origami Pores in Liposomes for Transmembrane Transport of Macromolecules. ACS Nano. 2021 Aug
382 24;15(8):12768-12779.

383 Funakoshi T, Clever M, Watanabe A, Imamoto N. Localization of Pom121 to the inner nuclear membrane
384 is required for an early step of interphase nuclear pore complex assembly. Mol Biol Cell. 2011
385 Apr;22(7):1058-69.

386 Huang Y, Wang T, Zhong L, Zhang W, Zhang Y, Yu X, Yuan S, Ni T. Molecular architecture of coronavirus
387 double-membrane vesicle pore complex. Nature. 2024 Sep;633(8028):224-231.

388 Kuyler GC, Barnard E, Cunningham RD, Sibariboyi S, White L, Wessels I, Smith MP, Motloung B,
389 Klumperman B. Amphiphilic Copolymers and Their Role in the Study of Membrane Proteins. J Phys Chem
390 Lett. 2025 Jun 12;16(23):5784-5799.

391 Jukic N, Perrino AP, Humbert F, Roux A, Scheuring S. Snf7 spirals sense and alter membrane curvature.
392 Nat Commun. 2022 Apr 21;13(1):2174.

393 Litschel T, Schwille P. Protein Reconstitution Inside Giant Unilamellar Vesicles. Annu Rev Biophys. 2021
394 May 6;50:525-548.

395 Liu S, Li S, Shen G, Sukumar N, Krezel AM, Li W. Structural basis of antagonizing the vitamin K catalytic
396 cycle for anticoagulation. Science. 2021 Jan 1;371(6524):eabc5667.

397 Matthaeus C, Sochacki KA, Dickey AM, Puchkov D, Haucke V, Lehmann M, Taraska JW. The molecular
398 organization of differentially curved caveolae indicates bendable structural units at the plasma
399 membrane. Nat Commun. 2022 Nov 24;13(1):7234.

400 McDowell MA, Heimes M, Fiorentino F, Mehmood S, Farkas Á, Coy-Vergara J, Wu D, Bolla JR, Schmid V,
401 Heinze R, Wild K, Flemming D, Pfeffer S, Schwappach B, Robinson CV, Sinning I. Structural Basis of Tail-
402 Anchored Membrane Protein Biogenesis by the GET Insertase Complex. Mol Cell. 2020 Oct 1;80(1):72-
403 86.e7.

404 Mercier V, Larios J, Molinard G, Goujon A, Matile S, Gruenberg J, Roux A. Endosomal membrane tension
405 regulates ESCRT-III-dependent intra-lumenal vesicle formation. Nat Cell Biol. 2020 Aug;22(8):947-959.

406 Morlot S, Galli V, Klein M, Chiaruttini N, Manzi J, Humbert F, Dinis L, Lenz M, Cappello G, Roux A.
407 Membrane shape at the edge of the dynamin helix sets location and duration of the fission reaction. Cell.
408 2012 Oct 26;151(3):619-29.

409 Nakamura S, Minamino T. Structure and Dynamics of the Bacterial Flagellar Motor Complex. Biomolecules.
410 2024 Nov 22;14(12):1488.

411 Ohi M, Li Y, Cheng Y, Walz T. Negative Staining and Image Classification - Powerful Tools in Modern
412 Electron Microscopy. Biol Proced Online. 2004;6:23-34.

413 Olivi L, Berger M, Creyghton RNP, De Franceschi N, Dekker C, Mulder BM, Claassens NJ, Ten Wolde PR,
414 van der Oost J. Towards a synthetic cell cycle. Nat Commun. 2021 Jul 26;12(1):4531.

415 Powers RE, Wang S, Liu TY, Rapoport TA. Reconstitution of the tubular endoplasmic reticulum network
416 with purified components. Nature. 2017 Mar 9;543(7644):257-260.

417 Prévost C, Tsai FC, Bassereau P, Simunovic M. Pulling Membrane Nanotubes from Giant Unilamellar
418 Vesicles. J Vis Exp. 2017 Dec 7;(130):56086.

419 Prévost C, Zhao H, Manzi J, Lemichez E, Lappalainen P, Callan-Jones A, Bassereau P. IRSp53 senses negative
420 membrane curvature and phase separates along membrane tubules. Nat Commun. 2015 Oct 15;6:8529.

421 Ranquin A, Van Gelder P. Maltoporin: sugar for physics and biology. Res Microbiol. 2004 Oct;155(8):611-
422 6.

423 Ripoll L, von Zastrow M, Blythe EE. Intersection of GPCR trafficking and cAMP signaling at
424 endomembranes. J Cell Biol. 2025 Apr 7;224(4):e202409027.

425 Salmonowicz H, Szczepanowska K. The fate of mitochondrial respiratory complexes in aging. Trends Cell
426 Biol. 2025 Mar 26:S0962-8924(25)00042-X.

427 Schöneberg J, Pavlin MR, Yan S, Righini M, Lee IH, Carlson LA, Bahrami AH, Goldman DH, Ren X, Hummer
428 G, Bustamante C, Hurley JH. ATP-dependent force generation and membrane scission by ESCRT-III and
429 Vps4. Science. 2018 Dec 21;362(6421):1423-1428.

430 Sligar SG, Denisov IG. Nanodiscs: A toolkit for membrane protein science. Protein Sci. 2021 Feb;30(2):297-
431 315.

432 Souza DP, Espadas J, Chaaban S, Moody ERR, Hatano T, Balasubramanian M, Williams TA, Roux A, Baum
433 B. Asgard archaea reveal the conserved principles of ESCRT-III membrane remodeling. Sci Adv. 2025 Feb
434 7;11(6):eads5255.

435 Stephan T, Brüser C, Deckers M, Steyer AM, Balzarotti F, Barbot M, Behr TS, Heim G, Hübner W, Ilgen P,
436 Lange F, Pacheu-Grau D, Pape JK, Stoldt S, Huser T, Hell SW, Möbius W, Rehling P, Riedel D, Jakobs S.
437 MICOS assembly controls mitochondrial inner membrane remodeling and crista junction redistribution to
438 mediate cristae formation. EMBO J. 2020 Jul 15;39(14):e104105.

439 Stephan T, Stoldt S, Barbot M, Carney TD, Lange F, Bates M, Bou Dib P, Inamdar K, Shcherbata HR,
440 Meinecke M, Riedel D, Dennerlein S, Rehling P, Jakobs S. Drosophila MIC10b can polymerize into cristae-
441 shaping filaments. Life Sci Alliance. 2024 Jan 22;7(4):e202302177.

442 Stępień P, Świątek S, Robles MYY, Markiewicz-Mizera J, Balakrishnan D, Inaba-Inoue S, De Vries AH, Beis
443 K, Marrink SJ, Heddle JG. CRAFTing Delivery of Membrane Proteins into Protocells using Nanodiscs. ACS
444 Appl Mater Interfaces. 2023 Nov 28;15(49):56689–701.

445 Strahl H, Ronneau S, González BS, Klutsch D, Schaffner-Barbero C, Hamoen LW. Transmembrane protein
446 sorting driven by membrane curvature. Nat Commun. 2015 Nov 2;6:8728.

447 Van de Cauter L, Fanalista F, van Buren L, De Franceschi N, Godino E, Bouw S, Danelon C, Dekker C,
448 Koenderink GH, Ganzinger KA. Optimized cDICE for Efficient Reconstitution of Biological Systems in Giant
449 Unilamellar Vesicles. ACS Synth Biol. 2021 Jul 16;10(7):1690-1702.

450 Van de Cauter L, Jawale YK, Tam D, Baldauf L, van Buren L, Koenderink GH, Dogterom M, Ganzinger KA.
451 High-Speed Imaging of Giant Unilamellar Vesicle Formation in cDICE. ACS Omega. 2024 Sep
452 25;9(41):42278-42288.

453 Verkman AS, Mitra AK. Structure and function of aquaporin water channels. Am J Physiol Renal Physiol.
454 2000 Jan;278(1):F13-28.

455 Voeltz GK, Prinz WA, Shibata Y, Rist JM, Rapoport TA. A class of membrane proteins shaping the tubular
456 endoplasmic reticulum. Cell. 2006 Feb 10;124(3):573-86.

457 Yvonnesdotter L, Rovšnik U, Blau C, Lycksell M, Howard RJ, Lindahl E. Automated simulation-based
458 membrane protein refinement into cryo-EM data. Biophys J. 2023 Jul 11;122(13):2773-2781.

459 Zubcevic L, Herzik MA Jr, Chung BC, Liu Z, Lander GC, Lee SY. Cryo-electron microscopy structure of the
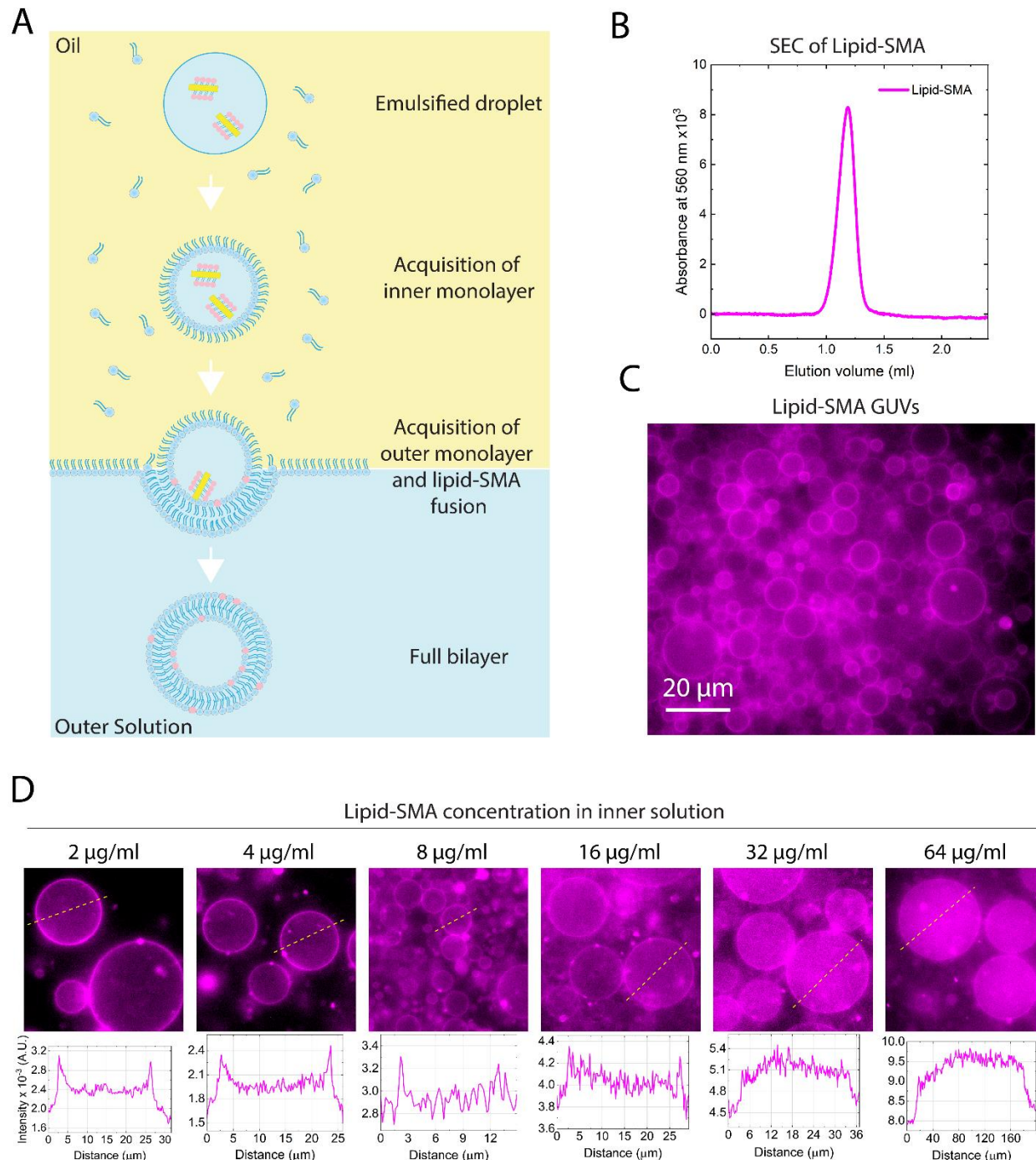460 TRPV2 ion channel. Nat Struct Mol Biol. 2016 Feb;23(2):180-186.

461

Figure 1: Lipid transfer from lipid-SMA to GUVs by the SMT approach. *(A): Schematic illustrating the SMT approach. The inner solution containing the lipid-SMA (visualized as pink phospholipids with a yellow belt) is emulsified in the oil phase containing lipids. The droplets progressively acquire the inner monolayer and the outer monolayer once they cross the oil/outer buffer interface. During this last step, the lipid-SMA fuse with the newly formed bilayer and their phospholipid content is incorporated into the GUV membrane. (B) Analytical size-exclusion chromatogram of lipid-SMA recorded at 560 nm, corresponding to DOPE-Rhodamine. (C): Typical field of view of GUVs generated by the SMT. The fluorescent signal, here shown in*

470   *magenta, originates from fluorescent phospholipids that were exclusively present in the lipid-SMA. (D):*

471   *GUVs generated using increasing concentration of lipid-SMA in the inner solution (indicated on top of the*

472   *images). The line scans visualize the extent of fluorescent lipid localization at the GUV membrane. The*

473   *fluorescent lipids originate exclusively from the lipid-SMA.*
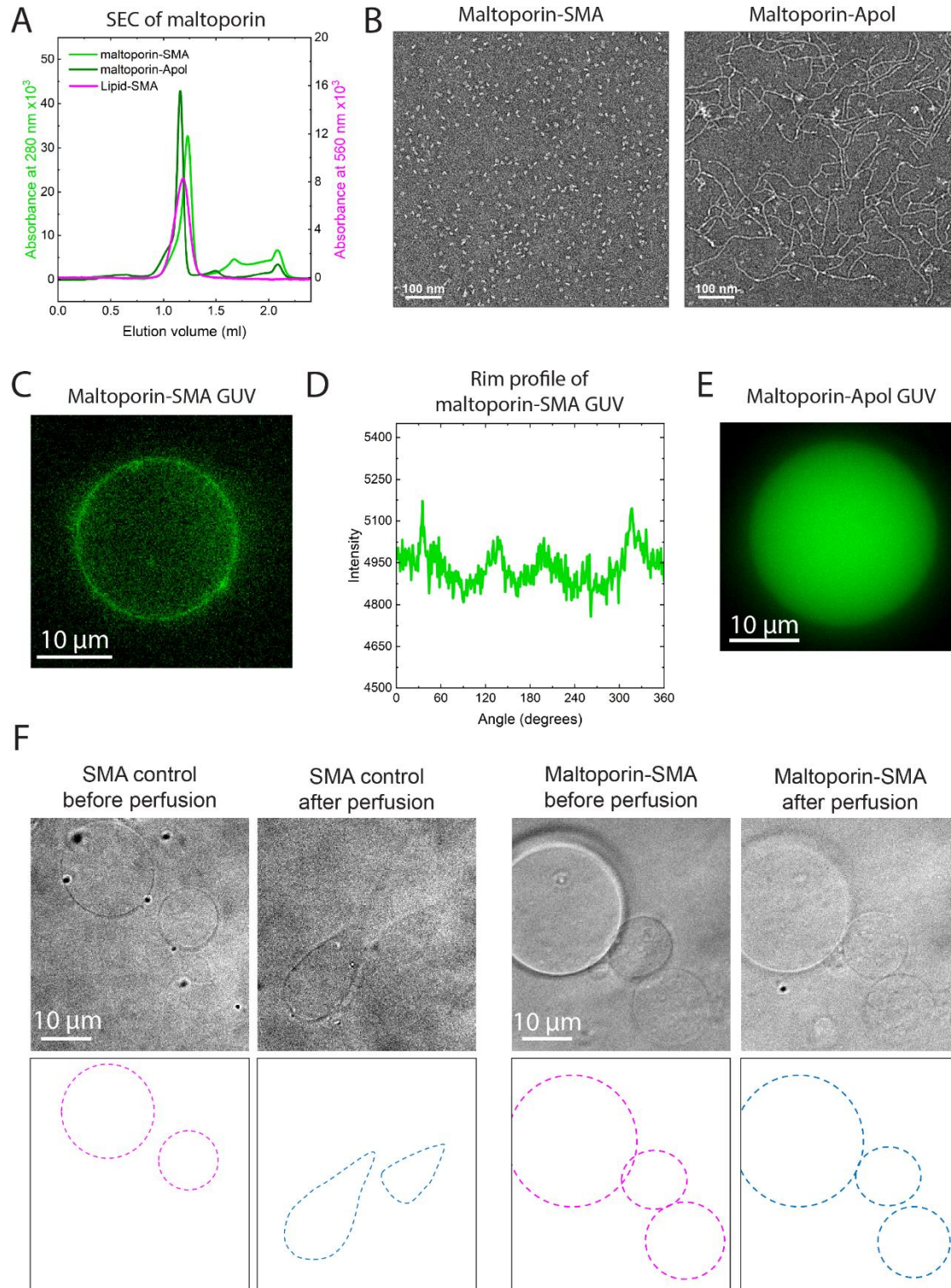
474

475

Figure 2: Maltoporin reconstitution in GUVs by the SMT approach. *(A): Analytical size-exclusion chromatogram of maltoporin-SMA and maltoporin-Apol recorded at 280 nm. Elution profile of lipid-SMA recorded at 560 nm is shown for comparison. (B): Negative-staining EM of maltoporin-SMA and maltoporin-Apol. While maltoporin-SMA gives a homogeneous population of individual particles,*

481   *reconstitution in Apol results in maltoporin filaments. (C): Example of GUV with reconstituted maltoporin-*
482   *SMA. (D): Rim profile of the GUV with reconstituted maltoporin-SMA shown in (C). (E): Example of GUV*
483   *with reconstituted maltoporin-Apol. (F): Functional assay of maltoporin-SMA reconstituted in GUVs.*
484   *Images of the same field of view before and after perfusion with hyperosmotic buffer containing 200 mM*
485   *maltose are shown. A control containing only SMA is shown. The schematics at the bottom clarify the*
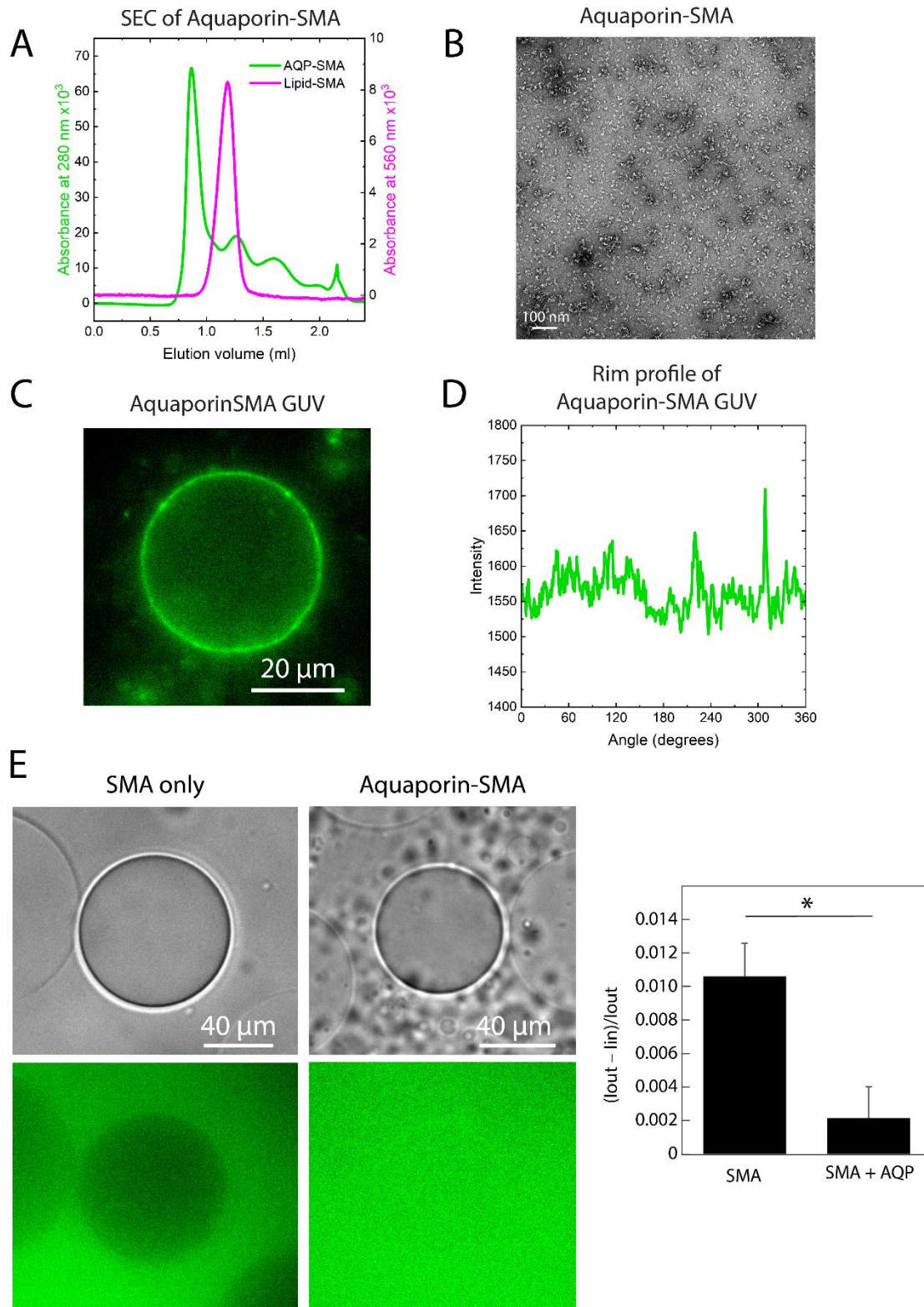486   *outline of the GUVs in each image. n=2.*

487

Figure 3: Aquaporin-12 reconstitution in GUVs by the SMT approach. *(A): Analytical size-exclusion chromatogram of AQP12-SMA recorded at 280 nm. Elution profile of lipid-SMA recorded at 560 nm is shown for comparison. (B): Negative-staining EM of AQP12-SMA. (C): Example of GUV with reconstituted*

491   *AQP12-SMA. (D): Rim scan of the GUV with reconstituted AQP12-SMA shown in (C). (E): Influx of H_2O_2 in*

492   *GUVs containing AQP-12-SMA or SMA-only control. The fluorescent signal from the H_2O_2 sensor is shown*

493   *in green. Presence of fluorescence signal inside the GUV lumen indicates that H_2O_2 has crossed the*

494   *membrane. The plot on the right shows the quantification of H_2O_2 permeation across the membrane, and*

495   *was calculated by normalizing the fluorescence intensity difference between inside and outside of each*

496   *GUV according to the formula: $I_{n,diff} = (I_{out} - I_{in})/I_{out}$ (see methods). p-value = 0.00116 (Mann-Whitney U*

497   *Test). n = 108 for AQP12-SMA; n = 200 for SMA-only control. Data were collected over 3 independent*

498   *experiments. For the details on the quantification, see methods.*
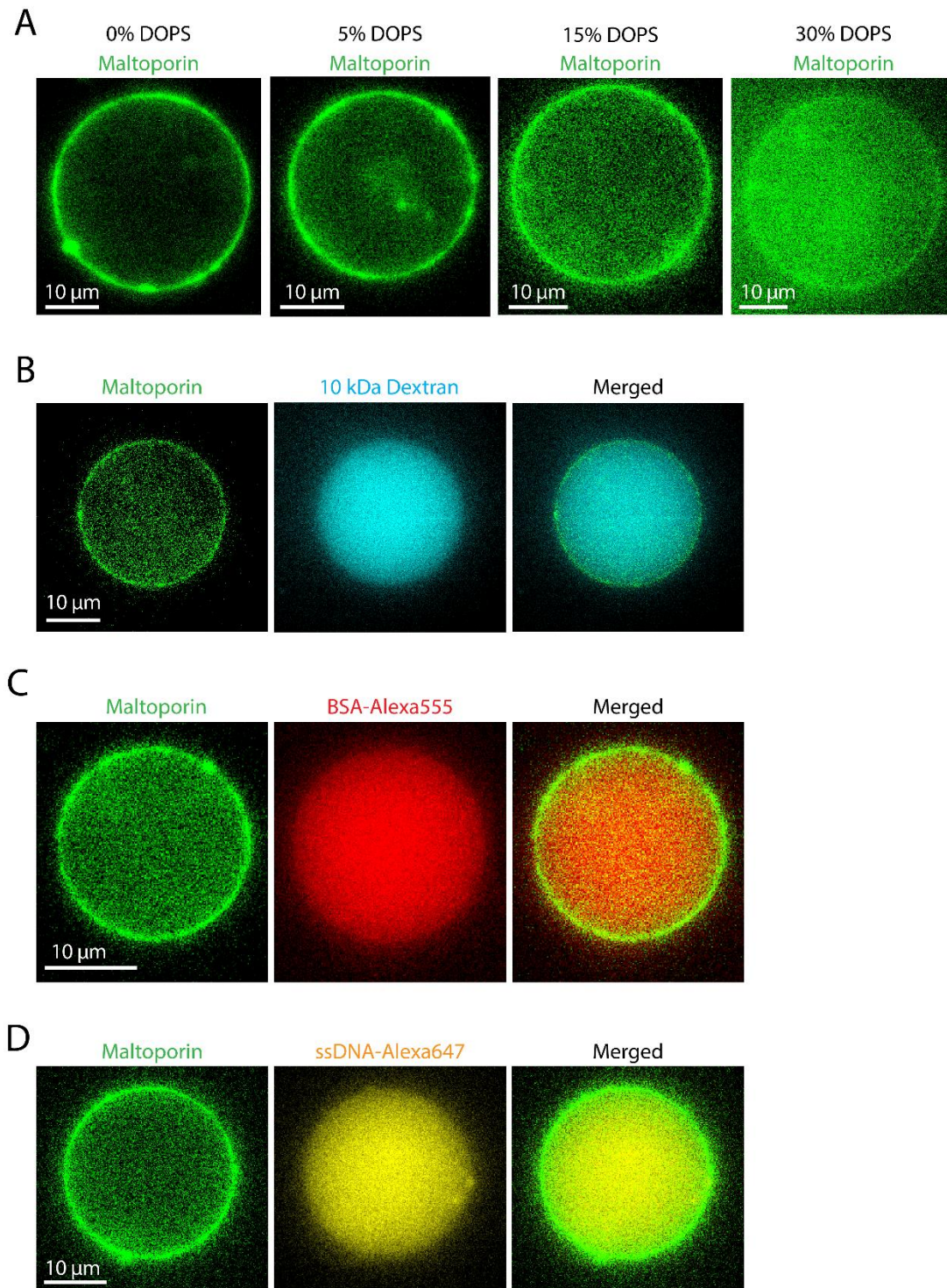
499

500

501

Figure 4: Transmembrane protein reconstitution in the presence of negatively charged lipids and upon co-encapsulation of macromolecules. *(A):* Reconstitution of maltoporin in GUVs containing an increasing amount of DOPS *in the GUV membrane. (B): Reconstitution of maltoporin upon co-encapsulation of 10-kDa Dextran-Alexa647. (C): Reconstitution of maltoporin upon co-encapsulation of BSA-Alexa555. (D): Reconstitution of maltoporin upon co-encapsulation of a 23-mer ssDNA-Alexa647.*

507
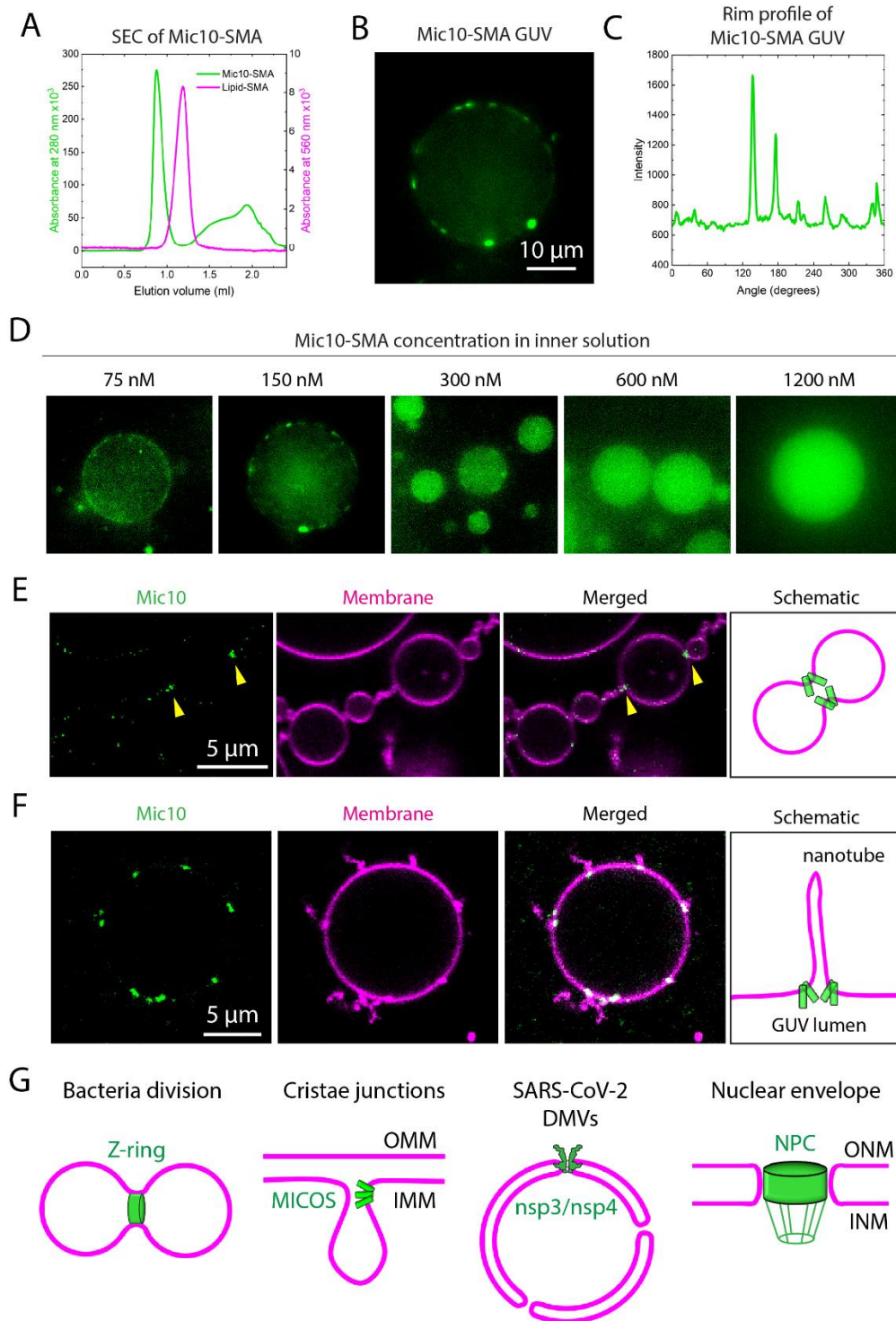
Figure 5: Mic10 reconstitution in GUVs by the SMT approach. *(A): Analytical size-exclusion chromatogram of Mic10-SMA recorded at 280 nm. Elution profile of lipid-SMA recorded at 560 nm is shown for comparison. (B): Example of spherical GUV with reconstituted Mic10-SMA. (C): Rim scan of the GUV with*

512   *reconstituted Mic10-SMA shown in (B). (D):* GUVs generated using increasing concentration of Mic10-SMA
513   in the inner solution *(the concentration used is indicated above the images). (E): Confocal image of*
514   *dumbbell-shaped GUVs having Mic10 cluster stably localized at catenoid necks (indicated by the yellow*
515   *arrowheads). For this experiment, DOPE-Rhodamine was included in the GUV membrane. (F): Confocal*
516   *image of spherical GUVs having Mic10 cluster stably localized at the nanotube necks emanating from the*
517   *GUV body. For this experiment, DOPE-Rhodamine was included in the GUV membrane. (G) Schematic*
518   *illustrating instances in which transmembrane proteins may play a role in curvature sensing at membrane*
519   *necks as part of larger protein complexes. The membrane is indicated in magenta; the relevant protein*
520   *complexes in green. OMM = outer mitochondrial membrane; IMM = inner mitochondrial membrane; DMVs*
521   *= double-membrane vesicles; ONM = outer nuclear membrane; INM = inner nuclear membrane; NPC =*
522   *nuclear pore complex.*

523